Time-Resolved Observation of Evolution of Amyloid-β Oligomer with Temporary Salt Crystals

Kichitaro Nakajima,[†] Tomoya Yamazaki,[‡] Yuki Kimura,[‡] Masatomo So,[¶] Yuji Goto,[¶] and Hirotsugu Ogi[*,§]

[†]*Global Center for Medical Engineering and Informatics, Osaka University, Suita, Osaka 565-0871, Japan*

[‡]*Institute of Low Temperature Science, Hokkaido University, Sapporo 060-8638, Japan*

[¶]*Institute of Protein Research, Osaka University, Suita, Osaka 565-0871, Japan*

[§]*Graduate School of Engineering, Osaka University, Suita, Osaka 565-0871, Japan*

E-mail: ogi@prec.eng.osaka-u.ac.jp

Phone: +81 (6)6879 7276. Fax: +81 (6)6879 7276

Abstract

The aggregation behavior of amyloid-β (Aβ) peptides remains unclarified despite the fact that it is closely related to the pathogenic mechanism of Alzheimer's disease. Aβ peptides form diverse oligomers with various diameters before nucleation, making clarification of the mechanism involved a complex problem with conventional macroscopic analysis methods. Time-resolved single-molecule level analysis in bulk solution is thus required to fully understand their early-stage aggregation behavior. Here, we perform time-resolved observation of the aggregation dynamics of Aβ oligomers in bulk solution using liquid-state transmission electron microscopy. Our observations reveal previously unknown behaviors. The most important discovery is that a salt crystal can precipitate even with a concentration much lower than its solubility, and it then dissolves in a short time, during which the aggregation reaction of Aβ peptides is significantly accelerated. These findings will provide new insights in the evolution of Aβ oligomer.

Graphical TOC Entry

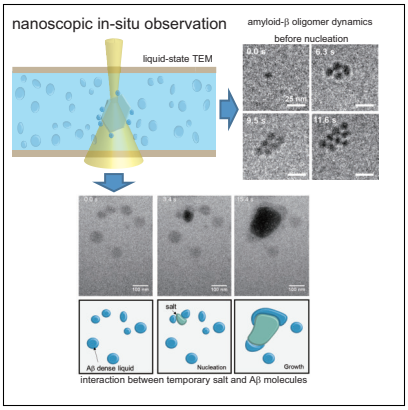

Keywords

amyloid-β oligomer, liquid-state TEM, salt crystal, aggregation acceleration

A great many studies have reported that aggregation of amyloid-β (Aβ) peptides is closely related to Alzheimer's disease.[1–3] Aβ peptides are produced from amyloid precursor protein[4] and form diverse aggregates through self-assembly, including low-molecular-weight aggregates (tetramers, hexamers, and dodecamers[5,6]), larger ($\sim$20 nm) oligomeric species,[7,8] and amyloid fibrils.[9,10] While neurotoxicity of amyloid fibrils has been indicated,[11,12] oligomeric disordered aggregates are also recognized as toxic materials; some recent studies[13,14] insist that their neurotoxicity is greater than that of fibrils. Therefore, it is critically important to clarify the oligomer evolution mechanism; however, this has never been straightforward because of the diversity of oligomers and the lack of a direct observation method for bulk solutions. The aggregation process for fibrils is essentially divided into an initial nucleation stage and a subsequent elongation stage.[15,16] The mechanism by which the latter occurs involves the addition of a monomer molecule to the fibril terminal, which occurs over a short time frame, allowing analysis with, for example, atomic force microscopy (AFM).[17] This fibril elongation behavior has been confirmed by countless studies that use well-established methods such as thioflavin-T fluorescence assay[18] and circular dichroism spectroscopy.[19] The fibrillation mechanism has thus been intensively investigated because of the speed at which it occurs and the existence of highly specific fluorescent material that can be used to study it.[20,21] However, the early-stage oligomer evolution before nucleation is poorly understood because of a lack of a similar effective fluorescent material, the length of time required for nucleation, and the diverse structures of oligomers; Aβ oligomers exist in a wide variety of sizes and structures, making it very difficult to fully clarify their evolutionary behavior by conventional methods. While recent NMR techniques[22,23] reveal the amyloid oligomerization behavior, they provide macroscopic information averaged over whole solution. AFM analysis allows for direct time-resolved observation within a restricted time only of the surface of a material,[24] but it fails to obtain structural information, unlike diffractometry.[25,26] Structural analysis and direct time-resolved observation at the single-molecule level are therefore needed to deeply understand the early-stage aggregation behavior of oligomers before nucleation.

In the present study, we succeeded in observing the early-stage evolution of oligomers from ∼5 nm in diameter in bulk solution using a liquid-state transmission electron microscopy (TEM) method,[27] which allows for the observation of the dynamics of nanoscale materials in bulk solutions, such as the aggregation of protein molecules[28,29] and the growth of carbon nanostructures.[30] Furthermore, the liquid-state TEM system allows acquisition not only of time-resolved nanoscale images, but also of electron diffraction (ED) patterns, providing structural information even of sub-ten-nanometer aggregates. It should be furthermore noted that the observation is achieved with a label-free manner without any fluorescence molecules; they affect the aggregation reaction,[31,32] preventing us from grasping the truth. Here, we report critical novel insights: (i) ∼5 nm particles of Aβ_{1-40} originate inside dense-liquid regions and join to form ∼100 nm amorphous beads, which specifically recognize each other and bind to form the network aggregates; (ii) long-distance specific interaction between bead aggregates is possible over distances of ∼10 nm; (iii) precipitation of protein aggregate can be promoted by the precipitation of salt crystals, and vice versa. These findings provide critically important information regarding the early-stage aggregation of Aβ peptides.

Liquid-state TEM observation was performed through the chip, inside which a 150-nm gold spacer was sandwiched between two SiN membranes as shown in Fig. S1. The actual thickness of the sample-solution layer reaches 650 nm at the center of the chip because of the bulge of the chip caused by a vacuum around the liquid cell.[33] Thus, the liquid cell mimics a bulk solution for aggregates in the early stage before nucleation, which are targets in this study, because their representative scale is mainly less than 100 nm as will be shown later. On the other hand, larger aggregates with the size over 100 nm might be suppressed their growth in the out-of-plane direction by the space limitation, being forced the in-plane elongation.

In this study, we set an electron flux of the beam to be typically ∼300 electrons·nm^{-2}s^{-1}. As for an impact of the electron-beam irradiation on the protein-molecule dynamics, we previously showed that it was negligible with its electron flux of 320 electrons·nm^{-2}s^{-1}:[29] lysozyme

crystals continuously grew under an electron-beam irradiation of 320 electrons·nm^{-2}s^{-1}, and its growth rate was identical to that without any electron dosage. Though, the crystals dissolved into a solution with the electron flux of 2,900 electrons·nm^{-2}s^{-1}. Based on these experimental results, our irradiation condition will not highly affect the aggregation reaction. Furthermore, we performed the intermissive observation to minimize the electron-beam effect as described in Supplementary Materials and Methods.

First, we observed the aggregation reaction of the Aβ_{1-40} peptide. The sample solution was prepared by filtering the original solution through a 200 nm membrane filter to remove larger aggregates formed during the initial sample preparation. No aggregate was found in the observable region in the first $\sim$1 h. Darkened regions then appeared, as shown in Fig. 1(a). Because of the TEM image, the darkened region indicates higher monomer concentration. Furthermore, solid-state aggregates are well highlighted with sharp edge and black color. We therefore hypothesize that the light darkened region observed in Fig. 1(a) indicates the dense-liquid regions in which the monomer concentration is higher than in the surrounding liquid. The presence of such regions may indicate liquid-liquid phase separation.[28,34] The small particles, which were even darker than the dark regions, then precipitated within the dense-liquid regions (Fig. 1(b)). This suggests that Aβ_{1-40} molecules coexist in three states in the first stage of the aggregation process, including soluble monomers, dense liquid, and small particles, all in one solution. The average diameter of the small particles is 5.9$\pm$1.3 nm (Fig. 1(c)). Bernstein and coworkers[5] reported the cross-sectional area of Aβ oligomers based on ion mobility analysis coupled with mass spectroscopy. According to their work, Aβ_{1-40} peptides preferably form tetramers with an equivalent diameter of 5.5 nm. This value is in line with the average diameter of the high-contrast particles found in the present study (inset in Fig. 1(b)), indicating that these high-contrast particles are tetramers of Aβ_{1-40}.

Then, the high-contrast particles gradually accumulated inside of the dense-liquid regions (Fig. 1(d)) and formed larger and lower-contrast bead-like aggregates with diameters between 100 and 200 nm (Fig. 1(e)), as shown in Movie S1 and Fig. S2. During this process,

some aggregates dissolved, while others grew: The dissolution and growth of the aggregates occurred in a synchronized manner, as shown in Fig. 1(f), indicating monomer movements among aggregates. The ED pattern of the resultant aggregate shown in Fig. 1(e) reveals that this aggregate is amorphous and lacks ordered structure (inset in Fig. 1(e)). These bead aggregates contacted each other, and the contact joint became smoother and thinner, and straighter structures were formed: Direct observations of this process are shown in Movie S2 and Fig. S3. Movie S2 shows the moment when a bead aggregate binds to a larger aggregate. Flattening occurs at the binding point (Fig. S3, 3.9-18.4 s). This aggregation procedure eventually resulted in the network-like aggregates shown in Fig. 1(g). We found that such aggregates also showed no diffraction point (i.e., they had no ordered structure), as shown in Fig. S4. The network-like aggregates are thus composed of many amorphous bead aggregates, linked via coalescence events. We expected subsequent formation of fibril-like aggregates, but no significant evolution was observed over the next 24 h in the entire observable area.

We also performed TEM observation for 10 μM Aβ_{1-42} solution. We found no aggregates in the first $\sim$30 min, and then found a small particle in the bulk solution, rather than in the dense-liquid region, as shown in Fig. 2(a). Similar particles appeared and formed a cluster. Figure 2(a) shows sequential snapshots of the generation of particles and their clustering behavior: The number of particles in each cluster increased to $\sim$10 within $\sim$10 s, as shown in Movie S3. The diameter of the clusters was approximately 30 nm. This initial aggregation behavior is obviously different from that of Aβ_{1-40} particles (inset in Fig. 1(b)), which appeared in the dense-liquid region and accumulated to form a larger amorphous bead-like aggregate (Fig. 1(e)). The average diameter of single Aβ_{1-42} particles was 8.3 nm (Fig. 2(b)), which is larger than that of Aβ_{1-40} particles. Based on comparison with the cross-sectional area reported by Bernstein and coworkers,[5] this diameter corresponds to that of a dodecamer. Therefore, the darkened particles that appeared initially are considered to be dodecamers of Aβ_{1-42}, which are critically important candidate toxic molecules in

Alzheimer's disease.[35,36]

Approximately 2 h after the observation experiment, we found aggregates of ∼30 nm diameter, as shown in Fig. 2(c), which are considered to be aggregates of dodecamers. The aggregates became clearer with time (Fig. 2(d)), and finally, the outline of the aggregate became very distinct, as shown in Fig. 2(e). In TEM images, higher contrast indicates a higher density in the case of amorphous particles. Thus, the density of dodecamer aggregates increased in the aggregation step shown in Fig. 2(c) to (e), as a result of coalescence among the aggregates and following their compactification via an anhydration process. Further incubation for ∼20 h caused aggregates with diffraction rings. Figure 2(f) is a TEM image of such an aggregate; its ED pattern (inset in Fig. 2(f)) shows a diffraction ring, indicating the formation of an ordered structure. Other aggregates showed clear diffraction spots with crystallographic lattice structures of 5.9 Å. These aggregates indicate the initiation of ordered structures with cross-β stacking at a spacing of 4.7 Å.[37] However, we again failed to observe a typical straight fibril-like aggregate even after a further 30 h incubation.

We observed highly specific interaction between the amorphous aggregates during the formation of the network-like aggregates through coalescence events in the Aβ_{1-40} solution: Figure 3(a) and Movie S4 reveal the strong interaction between the amorphous aggregates. A stick-like aggregate with a length and width of ∼90 nm and ∼30 nm, respectively, traveled straight across the observation view at a velocity of 500 nm/s and a rotation speed of 8 rad/s. It was, however, stopped suddenly near the aggregation branch, and its terminal attached to the branch end. The motion of the stick-like aggregate is explained in the schematic illustrations in Fig. 3(a). Thus, this binding reaction proceeds highly specifically. Figure 3(b) and Movie S5 show another binding reaction that demonstrates high specificity. The small bead aggregate indicated by the arrow in Fig. 3(b) bound to the far point, not to the nearest point. Furthermore, we did not observe any detachment event between aggregates once they were connected. This fact implies that these bindings of aggregates are specifically essentially, resulting in the formation of the network-like aggregates shown in

Fig. 1(g). These observations reveal that the oligomer species of Aβ_{1-40} peptide aggregate by recognizing corresponding binding sites in a highly specific manner.

In the present study, we added 100 mM NaCl to the sample solution to adjust the ion strength and accelerate the aggregation reaction. We found that salt crystals locally repeat precipitation and dissolution, as shown in Movie S6. It should be noted that the precipitation-dissolution event does occur despite the fact that the bulk concentration of NaCl in this study is lower than its solubility by a factor of 0.02. We consider that this phenomenon will be explained by the dynamic equilibration, where the precipitation reaction proceeds with a certain probability by the local density fluctuation, and the dissolution reaction occurs because of undersaturation. Figure S5(a) shows the two kinds of salt crystals observed in our experiments. One is rectangular in shape, as shown in Fig. S5(b); this was confirmed to be an NaCl crystal by its ED pattern, as shown in Fig. S5(c). The other type of crystal possesses hexagonal edges (lower part of Fig. S5(a)), but we were not able to acquire its ED pattern because it dissolved rapidly as shown in Movie S6. Based on the shape of the crystal and the composition of the phosphate-buffered saline solution—it is reported that phosphate salts show orthorhombic[38] and monoclinic[39] structures, not a cubic structure like NaCl—it is inferred that the crystal with hexagonal edges was a phosphate salt.

Important observations from this experiment are that (i) salt crystal dissolution accelerates the aggregation reaction of the proteins attached to the crystal surface, as shown in Movie S7; and (ii) a protein aggregate can promote salt nucleation, as shown in Fig. 4(a) and Movie S8. The former is especially important in the aggregation reaction: The acceleration of aggregation by the salt crystal is clarified in Movie S7, in which small aggregates are attracted to the surface of the salt crystal and condensed after the dissolution of the salt, resulting in $\sim$100 nm aggregates. Figure S6 and Movie S9 also show the promotion of the binding reaction between network-like aggregates by the salt crystal dissolution. In the sequential snapshots, the terminals of network-like aggregates bind to the surface of the phosphate salt crystal through hydrophobic interactions. The ends of the protein aggregates

attached to the salt crystal; then, the crystal shrinks during its dissolution, and the protein aggregates are connected at the vanishing point of the crystal. This event induces the assembly of the network aggregates. Schematic illustrations that explain these interactions are shown in Fig. S6.

The evolution of oligomer aggregates of Aβ_{1-40} and Aβ_{1-42}, based on observations in the present study, are summarized in Fig. 5. For Aβ_{1-40} (Fig. 5(a)), the aggregation reaction proceeds as follows: (i) Soluble monomers partially transform into the dense liquid state, where the monomer concentration increases; (ii) tetramers with an average diameter of 5.9 nm precipitate from the dense-liquid region; (iii) the tetramers in the dense-liquid region aggregate to form larger amorphous bead aggregates of approximately 100 nm; (iv) these bead aggregates interact with each other and become straighter rather than spherical through coalescence events, leading to the formation of network-like aggregates. These network-like disordered aggregates could be curvilinear fibrils,[40–43] which are metastable aggregates showing weak ThT emission formed with a much lower energy barrier than straight cross-β fibrils.

On the other hand, the aggregation reaction of Aβ_{1-42} (Fig. 5(b)) proceeds differently: (i) Monomers form dodecamers of 8.3 nm in diameter directly in the monomer phase, not in the dense-liquid region like Aβ_{1-40}. This can possibly be attributed to the greater tendency of Aβ_{1-42} to aggregate due to the two extra hydrophobic amino acids added to its C terminal.[44] (ii) Dodecamer clustering then occurs; the number of dodecamers in a single cluster of $\sim$50 nm diameter increases to $\sim$10 within approximately 10 s. (iii) The conformation of the clusters changes into ordered structures after a long lag time. It should be noted that although we observed some ordered aggregates with representative plane distances of 4-6 Å, we did not observe the typical straight amyloid fibrils at all in our experiments, despite a lengthy total observation time.

We succeeded in direct observation of the specific binding between early-stage oligomers. Importantly, the interaction distance appears to exceed 20 nm, as shown in Fig. 3(a) and (b),

and is therefore much longer than indicated by previous research: For example, Zhao and coworkers[45] calculated the interaction between Aβ molecules and their antibodies by setting the initial distance to be 3 Å in a molecular dynamics simulation. Furthermore, Zhou and coworkers[46] simulated structural changes of Aβ oligomers using a calculation setup in which the interaction distances of van der Waals force and electrostatic force were 8 and 14 Å, respectively. From these empirical values, it is expected that the long-distance interaction discovered in the present study cannot be explained directly by electrostatic, van der Waals, or hydrogen bond interactions. We suggest formation of bridges between stretched Aβ monomers held on surfaces of aggregates: Intrinsically disordered proteins, including Aβ peptides, transiently can stretch over dozens of nanometers as demonstrated with an AFM method,[47] and they could connect aggregates even with a distance of $\sim$20 nm. However, such thin stretching monomers extended from the aggregates, if any, are not observable with a frame rate of used TEM system.

It is well known that addition of NaCl promotes the precipitation of proteins, and the mechanism by which this occurs has been studied macroscopically and thermodynamically; NaCl absorbs the repulsive force which acts between the protein molecules by regulating ion strength.[48] Our observations provide new insight into the precipitation acceleration mechanism by salt, that is, local protein condensation due to repeated salt crystal precipitation and dissolution due to the dynamic equilibration, as shown in Fig. S6 and Movies S7 and S9.

Moreover, we found that early-stage Aβ aggregates promote precipitation of the salt crystal, as shown in Fig. 4(a) and Movie S8. Figure 4(b) depicts time-course curves of the representative length of an NaCl crystal in cases of nucleation from bulk solution and from the protein aggregation surface. The growth behavior of the salt crystal appears to take two steps: Precipitous growth within the first 0.2 s after nucleation, and subsequent slower growth. In the latter, the growth rate is about 24 nm/s, being independent of the nucleation point. The nucleation of NaCl is normally observable in a supersaturated solution. However,

we clearly observed a similar precipitation event even with a much lower NaCl concentration; the concentration we used was only 1% of equilibrium concentration. Furthermore, a growth rate of 24 nm/s is close to the values reported by Mullin[49] (65 nm/s) and Zhao et al.[50] (31.5 nm/s) upon macroscopic measurement in supersaturated solutions, suggesting a larger density fluctuation than typically thought. (We used different focusing length of electron beam in measuring Fig. 4(b), and furthermore the thickness of the sample solution was highly different among measuring positions due to bulging of the sample space as shown above; the actual energy absorbed in the solution is therefore highly ambiguous. Nevertheless, the growth rate here is close to the previously reported value, indicating that the electron irradiation effect is not dominant for the crystal growth.) Thus, precipitation events occur even in lower-concentration solutions in highly localized regions, although the precipitates are dissolved shortly afterwards. We then focused on the fast growth of the salt crystal within 0.2 s after nucleation. The growth rate was $\sim$100 nm/s and $\sim$300 nm/s with and without protein aggregate, respectively, or one order of magnitude larger than the growth rate outside of this brief time period. We believe that existing macroscopic methods cannot detect such rapid evolution of small particles ($<\sim$50 nm), and that this two-step growth reflects true precipitation behavior. The initial growth rate of NaCl crystals starting from the protein-aggregate surface is lower than that of crystals started from bulk solution by a factor of three. The difference in growth rates is caused by a difference of required driving forces for nucleation, which depends on interfacial energy between substrate and solute. Our result indicates that the interfacial energy between NaCl and Aβ_{1-40} is small enough for each to promote precipitation of the other and can be proof of cooperative interaction between protein aggregate and salt crystals.

Based on the above-mentioned findings, we suggest a nanoscopic autocatalytic-like aggregation mechanism for Aβ peptide through the precipitation-dissolution of salt crystals, as shown in Fig. 4(c): The protein-aggregate surface promotes salt nucleation by decreasing the apparent activation energy barrier for nucleation by reducing the interfacial energy, then

the salt crystal grows, attracting protein aggregates to its surface. The crystal eventually shrinks during dissolution so that the aggregates condense at its vanishing point. Previous studies[51,52] demonstrated the importance of the liquid-solid interface or the gas-liquid interface as the monomer adsorber; the interfaces dramatically accelerate the aggregation process of amyloidogenic proteins. Furthermore, we previously showed that the shrinking interface highly promotes the nucleation reaction of protein aggregates through the local condensation of the attached proteins,[53–55] as illustrated in Fig. S7: Ultrasonic cavitation, i.e. a dynamic gas-liquid interface, is generated by the negative pressure of the ultrasonic pressure and repeats the expansion and shrink events along with pressure fluctuation of the ultrasonic field. The peptides are attached on the interface during the expansion phase. The bubble thereafter collapses by the positive pressure of ultrasonic wave and shrinks toward its center. Then, the peptide molecules follow the interface movement, and they are condensed at the vanishing point of the bubble, where acceleration of the aggregation reaction is made possible. The temporary salt crystals also provide the solid-liquid interface during the growth phase, on which Aβ peptides and small aggregates are attached, and it shrinks during the dissolution phase, and the attached proteins are condensed at the vanishing point. This autocatalytic-like aggregation model with temporary salt crystal is illustrated in Fig. 4(c).

Finally, we mention about the electron-beam dose effect on our observations. The dose rate adopted in this study ($\sim$300 electrons$\cdot$nm^{-2}s^{-1}) caused insignificant influence on the growth behavior of lysozyme crystals,[29] and we performed the intermissive observation to further minimize the dose effect in this study, resulting in the growth rate of the salt crystal close to those evaluated by macroscopic experiments. However, because some studies[28,56–59] indicate certain dose effect on growth rates of nanostructures with dose rates, which are comparable with or smaller than our dose rate, we will investigate the dose effect in more detail in our future study.

Materials and Methods

Preparation of Aβ sample

Lyophilized A$\beta_{1-40/1-42}$ powder was purchased from the Peptide Institute (Aβ_{1-40}: 4307-v, Aβ_{1-42}: 4349-v, Japan). Aβ peptide powder was dissolved in dimethyl-sulfoxide (DMSO) and stirred at 200 rpm with a magnetic stirrer. Then, the solution was diluted with phosphate-buffered saline (PBS, pH 7.4) with 100 mM NaCl to a final peptide concentration of 10 μM. The concentration of DMSO remains 20% in a sample solution. The sample solution was filtrated through a membrane filter with a pore diameter of 200 nm just before addition to an observation chip. All chemicals were purchased from Wako Pure Chemical Industries, Ltd (Japan).

Liquid-state TEM observation

We used the JEOL transmission electron microscope system, JEM-2100F, with an acceleration voltage of 200 kV. Typical electron flux is $\sim$300 electron nm^{-2} s^{-1}, which was calculated from the total current of the electron beam in a blank sample, as measured with a combination of a Faraday gauge (JEOL Ltd.) and a picoammeter (Model 6485; Keithley Instruments, Inc., Cleveland, OH), divided by the area of the electron beam at the observation point. Movies were recorded with a JEOL CMOS camera system (EM-Z15327TCMOS) with an acquisition rate of 5 or 30 fps, depending on the area of interest. For liquid-state TEM observation, we used a TEM holder with a liquid cell system (Poseidon Select, Protochips, USA) to make a thin liquid layer with a spacer with a thickness of 150 nm. It is important to note that the actual thickness of the liquid layer was greater than 150 nm because the SiN membrane is pulled by the vacuum.[33] To introduce sample solution into a highly vacuumed chamber for observation, the chips were treated to be hydrophilic as previously described.[29] The appearance of used chips (EPW-55W & EPB-55DS, Protochips, USA) and an overview of the observation system are shown in Fig. S1. Observation was performed

for ∼30 h for each sample solution. Details about the experimental procedure appear in the Supplementary Materials and Methods.

Acknowledgement

The authors are grateful to professors Hisashi Okumura and Satoru Itoh (National Institute of Natural Sciences, Okazaki, Japan) for valuable comments on the long-distance interactions between oligomers.

Supporting Information Available

The following files are available free of charge.

- Supplementary Material: The file includes supplementary figures, Fig. S1-Fig. S7.
- Movie S1: Accumulation of tetramers precipitated from the dense-liquid region and formation of the amorphous bead aggregates.
- Movie S2: Coalescence event between a spherical amorphous aggregate and larger aggregate.
- Movie S3: Clustering behavior of Aβ_{1-42} particles.
- Movie S4: Highly specific interaction between amorphous aggregates.
- Movie S5: Specific binding of a small bead aggregate to the larger aggregate.
- Movie S6: Precipitation-dissolution events of salt crystals.
- Movie S7: Condensation of peptides induced by the dissolution event of a salt crystal.
- Movie S8: Precipitation of salt crystal by the aggregate of Aβ peptides.

- Movie S9: The terminal connection event of the network-like aggregates caused during dissolution of the salt crystal.

References

(1) Glenner, G. G.; Wong, C. W. Alzheimer's disease: Initial report of the purification and characterization of a novel cerebrovascular amyloid protein. *Biochem. Biophys. Res. Commun.* **1984**, *120*, 885 – 890.

(2) Masters, C. L.; Simms, G.; Weinman, N. A.; Multhaup, G.; McDonald, B. L.; Beyreuther, K. Amyloid plaque core protein in Alzheimer disease and Down syndrome. *Proc. Natl. Acad. Sci. USA* **1985**, *82*, 4245–4249.

(3) Salvadores, N.; Shahnawaz, M.; Scarpini, E.; Tagliavini, F.; Soto, C. Detection of misfolded Aβ oligomers for sensitive biochemical diagnosis of Alzheimer's disease. *Cell Rep.* **2014**, *7*, 261 – 268.

(4) Vassar, R.; Bennett, B. D.; Babu-Khan, S.; Kahn, S.; Mendiaz, E. A.; Denis, P.; Teplow, D. B.; Ross, S.; Amarante, P.; Loeloff, R. et al. β-secretase cleavage of Alzheimer's amyloid precursor protein by the transmembrane aspartic protease BACE. *Science* **1999**, *286*, 735–741.

(5) Bernstein, S. L.; Dupuis, N. F.; Lazo, N. D.; Wyttenbach, T.; Condron, M. M.; Bitan, G.; Teplow, D. B.; Shea, J. E.; Ruotolo, B. T.; Robinson, C. V. et al. Amyloid-β protein oligomerization and the importance of tetramers and dodecamers in the aetiology of Alzheimer's disease. *Nat. Chem.* **2009**, *1*, 326–331.

(6) Economou, N. J.; Giammona, M. J.; Do, T. D.; Zheng, X.; Teplow, D. B.; Buratto, S. K.; Bowers, M. T. Amyloid β-protein assembly and Alzheimer's disease: dodecamers of Aβ42, but not of Aβ40, seed fibril formation. *J. Am. Chem. Soc.* **2016**, *138*, 1772–1775.

(7) Stroud, J. C.; Liu, C.; Teng, P. K.; Eisenberg, D. Toxic fibrillar oligomers of amyloid-β have cross-β structure. *Proc. Natl. Acad. Sci. USA* **2012**, *109*, 7717–7722.

(8) Shea, D.; Hsu, C.-C.; Bi, T. M.; Paranjapye, N.; Childers, M. C.; Cochran, J.; Tomberlin, C. P.; Wang, L.; Paris, D.; Zonderman, J. et al. α-sheet secondary structure in amyloid β-peptide drives aggregation and toxicity in Alzheimer's disease. *Proc. Natl. Acad. Sci. USA* **2019**, *116*, 8895–8900.

(9) Lührs, T.; Ritter, C.; Adrian, M.; Riek-Loher, D.; Bohrmann, B.; Döbeli, H.; Schubert, D.; Riek, R. 3D structure of Alzheimer's amyloid-β_{1-42} fibrils. *Proc. Natl. Acad. Sci. USA* **2005**, *102*, 17342–17347.

(10) Lee, J.; Culyba, E. K.; Powers, E. T.; Kelly, J. W. Amyloid-β forms fibrils by nucleated conformational conversion of oligomers. *Nat. Chem. Biol.* **2011**, *7*, 602–609.

(11) Hardy, J.; Higgins, G. Alzheimer's disease: the amyloid cascade hypothesis. *Science* **1992**, *256*, 184–185.

(12) Lorenzo, A.; Yankner, B. A. Amyloid fibril toxicity in Alzheimer's disease and diabetes. *Ann. NY Acad. Sci.* **1996**, *777*, 89–95.

(13) Balducci, C.; Beeg, M.; Stravalaci, M.; Bastone, A.; Sclip, A.; Biasini, E.; Tapella, L.; Colombo, L.; Manzoni, C.; Borsello, T. et al. Synthetic amyloid-β oligomers impair long-term memory independently of cellular prion protein. *Proc. Natl. Acad. Sci. USA* **2010**, *107*, 2295–2300.

(14) He, Y.; Zheng, M.-M.; Ma, Y.; Han, X.-J.; Ma, X.-Q.; Qu, C.-Q.; Du, Y.-F. Soluble oligomers and fibrillar species of amyloid β-peptide differentially affect cognitive functions and hippocampal inflammatory response. *Biochem. Biophys. Res. Commun.* **2012**, *429*, 125 – 130.

(15) Kato, M.; Kinoshita, H.; Enokita, M.; Hori, Y.; Hashimoto, T.; Iwatsubo, T.; Toyo'oka, T. Analytical method for β-amyloid fibrils using CE-laser induced fluorescence and its application to screening for inhibitors of β-amyloid protein aggregation. *Anal. Chem.* **2007**, *79*, 4887–4891.

(16) Morris, A. M.; Watzky, M. A.; Finke, R. G. Protein aggregation kinetics, mechanism, and curve-fitting: A review of the literature. *Biochim. Biophys. Acta (BBA) - Proteins and Proteomics* **2009**, *1794*, 375 – 397.

(17) Banerjee, S.; Hashemi, M.; Lv, Z.; Maity, S.; Rochet, J. C.; Lyubchenko, Y. L. A novel pathway for amyloids self-assembly in aggregates at nanomolar concentration mediated by the interaction with surfaces. *Sci. Rep.* **2017**, *7*, 1–11.

(18) Biancalana, M.; Koide, S. Molecular mechanism of thioflavin-T binding to amyloid fibrils. *Biochim. Biophys. Acta (BBA) - Proteins and Proteomics* **2010**, *1804*, 1405 – 1412.

(19) Woody, R. W. Circular dichroism. *Methods in Enzymol.* **1995**, *246*, 34 – 71.

(20) Ogi, H.; Fukushima, M.; Hamada, H.; Noi, K.; Hirao, M.; Yagi, H.; Goto, Y. Ultrafast propagation of β-amyloid fibrils in oligomeric cloud. *Sci. Rep.* **2015**, *4*, 6960.

(21) Ogi, H.; Fukushima, M.; Uesugi, K.; Yagi, H.; Goto, Y.; Hirao, M. Acceleration of deposition of Aβ_{1-40} peptide on ultrasonically formed Aβ_{1-40} nucleus studied by wireless quartz-crystal-microbalance biosensor. *Biosens. Bioelectron.* **2013**, *40*, 200 – 205.

(22) Barnes, C. A.; Robertson, A. J.; Louis, J. M.; Anfinrud, P.; Bax, A. Observation of β-amyloid peptide oligomerization by pressure-jump NMR spectroscopy. *J. Am. Chem. Soc.* **2019**, *141*, 13762–13766.

(23) Kotler, S. A.; Brender, J. R.; Vivekanandan, S.; Suzuki, Y.; Yamamoto, K.; Monette, M.; Krishnamoorthy, J.; Walsh, P.; Cauble, M.; Holl, M. M. et al. High-resolution

NMR characterization of low abundance oligomers of amyloid-β without purification. *Sci. Rep.* **2015**, *5*, 1–12.

(24) Watanabe-Nakayama, T.; Ono, K.; Itami, M.; Takahashi, R.; Teplow, D. B.; Yamada, M. High-speed atomic force microscopy reveals structural dynamics of amyloid β_{1-42} aggregates. *Proc. Natl. Acad. Sci. USA* **2016**, *113*, 5835–5840.

(25) Lane, R. E.; Korbie, D.; Anderson, W.; Vaidyanathan, R.; Trau, M. Analysis of exosome purification methods using a model liposome system and tunable-resistive pulse sensing. *Sci. Rep.* **2015**, *5*.

(26) Laganowsky, A.; Liu, C.; Sawaya, M. R.; Whitelegge, J. P.; Park, J.; Zhao, M.; Pensalfini, A.; Soriaga, A. B.; Landau, M.; Teng, P. K. et al. Atomic view of a toxic amyloid small oligomer. *Science* **2012**, *335*, 1228–1231.

(27) De Jonge, N.; Ross, F. M. Electron microscopy of specimens in liquid. *Nat. Nanotech.* **2011**, *6*, 695–704.

(28) Le Ferrand, H.; Duchamp, M.; Gabryelczyk, B.; Cai, H.; Miserez, A. Time-resolved observations of liquid-iquid phase separation at the nanoscale using in situ liquid transmission electron microscopy. *J. Am. Chem. Soc.* **2019**, *141*, 7202–7210.

(29) Yamazaki, T.; Kimura, Y.; Vekilov, P. G.; Furukawa, E.; Shirai, M.; Matsumoto, H.; Van Driessche, A. E. S.; Tsukamoto, K. Two types of amorphous protein particles facilitate crystal nucleation. *Proc. Natl. Acad. Sci. USA* **2017**, *114*, 2154–2159.

(30) Bahri, M.; Dembélé, K.; Sassoye, C.; Debecker, D. P.; Moldovan, S.; Gay, A. S.; Hirlimann, C.; Sanchez, C.; Ersen, O. In situ insight into the unconventional ruthenium catalyzed growth of carbon nanostructures. *Nanoscale* **2018**, *10*, 14957–14965.

(31) D'Amico, M.; Di Carlo, M. G.; Groenning, M.; Militello, V.; Vetri, V.; Leone, M.

Thioflavin T promotes Aβ_{1-40} amyloid fibrils formation. *J. Phys. Chem. Lett.* **2012**, *3*, 1596–1601.

(32) Kumar, H.; Singh, J.; Kumari, P.; Udgaonkar, J. B. Modulation of the extent of structural heterogeneity in α-synuclein fibrils by the small molecule thioflavin T. *J. Biol. Chem.* **2017**, *292*, 16891–16903.

(33) Holtz, M. E.; Yu, Y.; Gao, J.; Abruña, H. D.; Muller, D. A. In situ electron energy-loss spectroscopy in liquids. *Microsc. Microanal.* **2013**, *19*, 1027–1035.

(34) Alberti, S.; Gladfelter, A.; Mittag, T. Considerations and challenges in studying liquid-liquid phase separation and biomolecular condensates. *Cell* **2019**, *176*, 419 – 434.

(35) Lesné, S.; Ming, T. K.; Kotilinek, L.; Kayed, R.; Glabe, C. G.; Yang, A.; Gallagher, M.; Ashe, K. H. A specific amyloid-β protein assembly in the brain impairs memory. *Nature* **2006**, *440*, 352–357.

(36) Cheng, I. H.; Scearce-Levie, K.; Legleiter, J.; Palop, J. J.; Gerstein, H.; Bien-Ly, N.; Puoliväli, J.; Lesné, S.; Ashe, K. H.; Muchowski, P. J. et al. Accelerating amyloid-β fibrillization reduces oligomer levels and functional deficits in Alzheimer disease mouse models. *J. Biol. Chem.* **2007**, *282*, 23818–23828.

(37) Eisenberg, D.; Jucker, M. The amyloid state of proteins in human diseases. *Cell* **2012**, *148*, 1188 – 1203.

(38) Catti, M.; Ferraris, G.; Franchini-Angela, M. The crystal structure of $Na_2HPO_42H_2O$. Competition between coordination and hydrogen bonds. *Acta Crystallogr. B Struct. Cryst. Cryst. Chem.* **1977**, *33*, 3449–3452.

(39) Baur, W. H.; Khan, A. A. On the crystal chemistry of salt hydrates. VI. The crystal structures of disodium hydrogen orthoarsenate heptahydrate and of disodium hydrogen

orthophosphate heptahydrate. *Acta Crystallogr. B Struct. Cryst. Cryst. Chem.* **1970**, *26*, 1584–1596.

(40) Foley, J.; Hill, S. E.; Miti, T.; Mulaj, M.; Ciesla, M.; Robeel, R.; Persichilli, C.; Raynes, R.; Westerheide, S.; Muschol, M. Structural fingerprints and their evolution during oligomeric vs. oligomer-free amyloid fibril growth. *J. Chem. Phys.* **2013**, *139*, 121901.

(41) Miti, T.; Mulaj, M.; Schmit, J. D.; Muschol, M. Stable, metastable, and kinetically trapped amyloid aggregate phases. *Biomacromol.* **2015**, *16*, 326–335.

(42) Hasecke, F.; Miti, T.; Perez, C.; Barton, J.; Schölzel, D.; Gremer, L.; Grüning, C. S. R.; Matthews, G.; Meisl, G.; Knowles, T. P. J. et al. Origin of metastable oligomers and their effects on amyloid fibril self-assembly. *Chem. Sci.* **2018**, *9*, 5937–5948.

(43) Perez, C.; Miti, T.; Hasecke, F.; Meisl, G.; Hoyer, W.; Muschol, M.; Ullah, G. Mechanism of fibril and soluble oligomer formation in amyloid beta and hen egg white lysozyme proteins. *J. Phys. Chem. B* **2019**, *123*, 5678–5689.

(44) Chakraborty, S.; Das, P. Emergence of alternative structures in amyloid beta_{1-42} monomeric landscape by N-terminal hexapeptide amyloid inhibitors. *Sci. Rep.* **2017**, *7*, 1–12.

(45) Zhao, J.; Nussinov, R.; Ma, B. Mechanisms of recognition of amyloid-β (Aβ) monomer, oligomer, and fibril by homologous antibodies. *J. Biol. Chem.* **2017**, *292*, 18325–18343.

(46) Zhou, X.; Xu, J. Free cholesterol induces higher β-sheet content in Aβ oligomers by aromatic interaction with Phe19. *PLOS ONE* **2012**, *7*, 1–8.

(47) Zhang, Y.; Hashemi, M.; Lv, Z.; Williams, B.; Popov, K. I.; Dokholyan, N. V.; Lyubchenko, Y. L. High-speed atomic force microscopy reveals structural dynamics of α-synuclein monomers and dimers. *J. Chem. Phys.* **2018**, *148*, 123322.

(48) Hill, S. E.; Miti, T.; Richmond, T.; Muschol, M. Spatial extent of charge repulsion regulates assembly pathways for lysozyme amyloid fibrils. *PLOS ONE* **2011**, *6*, 1–12.

(49) Mullin, J. W. Crystallization, Third Edition. *Chemie Ingenieur Technik* **1998**, *70*, 1468.

(50) Zhao, J.; Miao, H.; Duan, L.; Kang, Q.; He, L. The mass transfer process and the growth rate of NaCl crystal growth by evaporation based on temporal phase evaluation. *Opt. Lasers Eng.* **2012**, *50*, 540 – 546, Computational Optical Measurement.

(51) Banerjee, S.; Hashemi, M.; Lv, Z.; Maity, S.; Rochet, J. C.; Lyubchenko, Y. L. A novel pathway for amyloids self-assembly in aggregates at nanomolar concentration mediated by the interaction with surfaces. *Sci. Rep.* **2017**, *7*, 1–11.

(52) Pan, Y.; Banerjee, S.; Zagorski, K.; Shlyakhtenko, L. S.; Kolomeisky, A. B.; Lyubchenko, Y. L. Molecular model for the surface-catalyzed protein self-assembly. *J. Phys. Chem. B* **2020**, *124*, 366–372.

(53) Nakajima, K.; Ogi, H.; Adachi, K.; Noi, K.; Hirao, M.; Yagi, H.; Goto, Y. Nucleus factory on cavitation bubble for amyloid β fibril. *Sci. Rep.* **2016**, *6*, 1–10.

(54) Nakajima, K.; Nishioka, D.; Hirao, M.; So, M.; Goto, Y.; Ogi, H. Drastic acceleration of fibrillation of insulin by transient cavitation bubble. *Ultrason. Sonochem.* **2017**, *36*, 206–211.

(55) Nakajima, K.; So, M.; Takahashi, K.; Tagawa, Y. I.; Hirao, M.; Goto, Y.; Ogi, H. Optimized ultrasonic irradiation finds out ultrastable Aβ_{1-40} oligomers. *J. Phys. Chem. B* **2017**, *121*, 2603–2613.

(56) Zhang, Y.; Keller, D.; Rossell, M. D.; Erni, R. Formation of Au nanoparticles in liquid cell transmission electron microscopy: From a systematic study to engineered nanostructures. *Chem. Mater.* **2017**, *29*, 10518–10525.

(57) Schneider, N. M.; Norton, M. M.; Mendel, B. J.; Grogan, J. M.; Ross, F. M.; Bau, H. H. Electron–water interactions and implications for liquid cell electron microscopy. *J. Phys. Chem. C* **2014**, *118*, 22373–22382.

(58) Mirsaidov, U. M.; Zheng, H.; Bhattacharya, D.; Casana, Y.; Matsudaira, P. Direct observation of stick-slip movements of water nanodroplets induced by an electron beam. *Proc. Natl. Acad. Sci. USA* **2012**, *109*, 7187–7190.

(59) Grogan, J. M.; Schneider, N. M.; Ross, F. M.; Bau, H. H. Bubble and pattern formation in liquid induced by an electron beam. *Nano Let.* **2014**, *14*, 359–364.

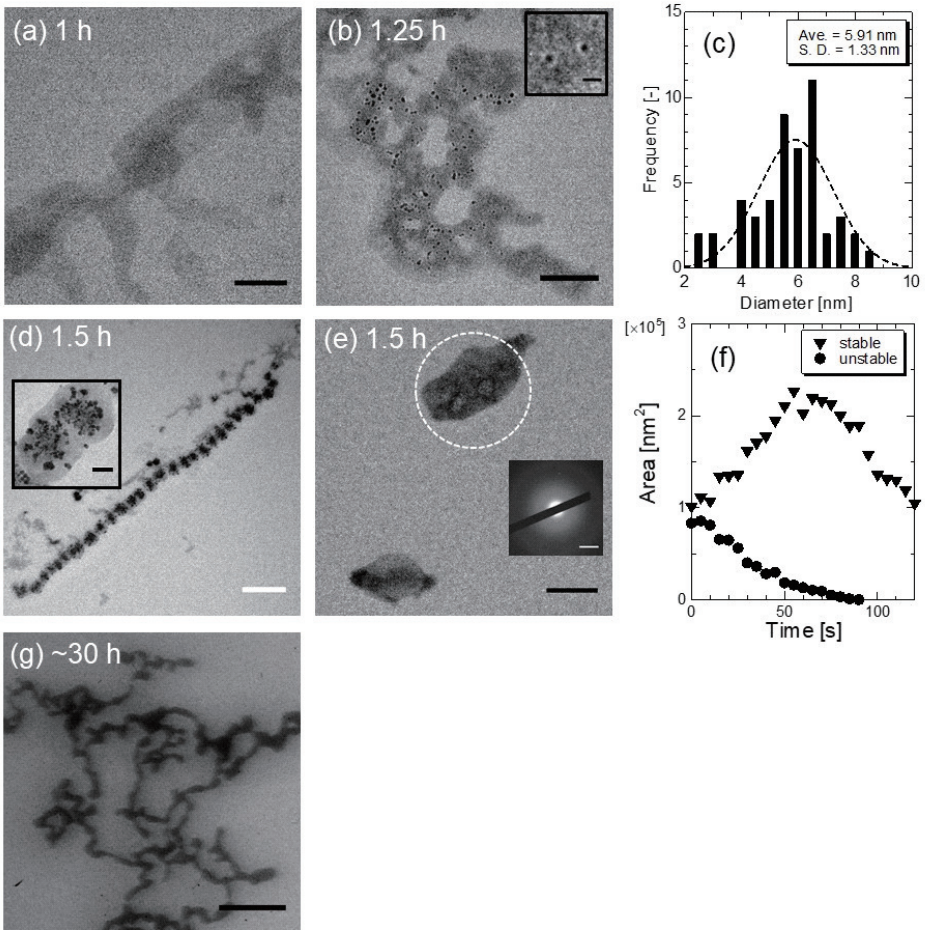

Figure 1: Evolution of aggregation of Aβ_{1-40} peptides. (a) A TEM image showing a dense-liquid region of Aβ_{1-40} peptide. The scale bar denotes 100 nm. (b) Small particles precipitated from the dense-liquid region. Scale bars in the main image and inset denote 100 nm and 10 nm, respectively. (c) Distribution of the diameter of the small particles precipitated from the dense-liquid region, which was obtained from ∼50 particles in images at 1.25 h, including Fig. 1(b). The dashed line depicts the fitting curve drawn by the Gaussian function. (d) The dense-liquid region containing the high-contrast particles. The inset shows an enlarged view. Scale bars in the main image and enlarged image denote 500 nm and 50 nm, respectively. (e) Amorphous bead-like aggregates resulted from the small particles in (d) through their condensation process demonstrated in Movie S1. Inset shows the ED pattern of the aggregate inside the white dashed circle. Scale bars in the TEM image and ED pattern denote 200 nm and 3 nm^{-1}, respectively. (f) Synchronized dissolution and growth behavior of the dense-liquid region together with the small particles. (g) Network-like aggregates formed through coalescence of bead aggregates. The scale bar denotes 200 nm. Figures (a), (b), and (g) are taken from different positions, while Figures (d) and (e) are from the same position (their details are shown in Fig. S2 and Movie S1.)

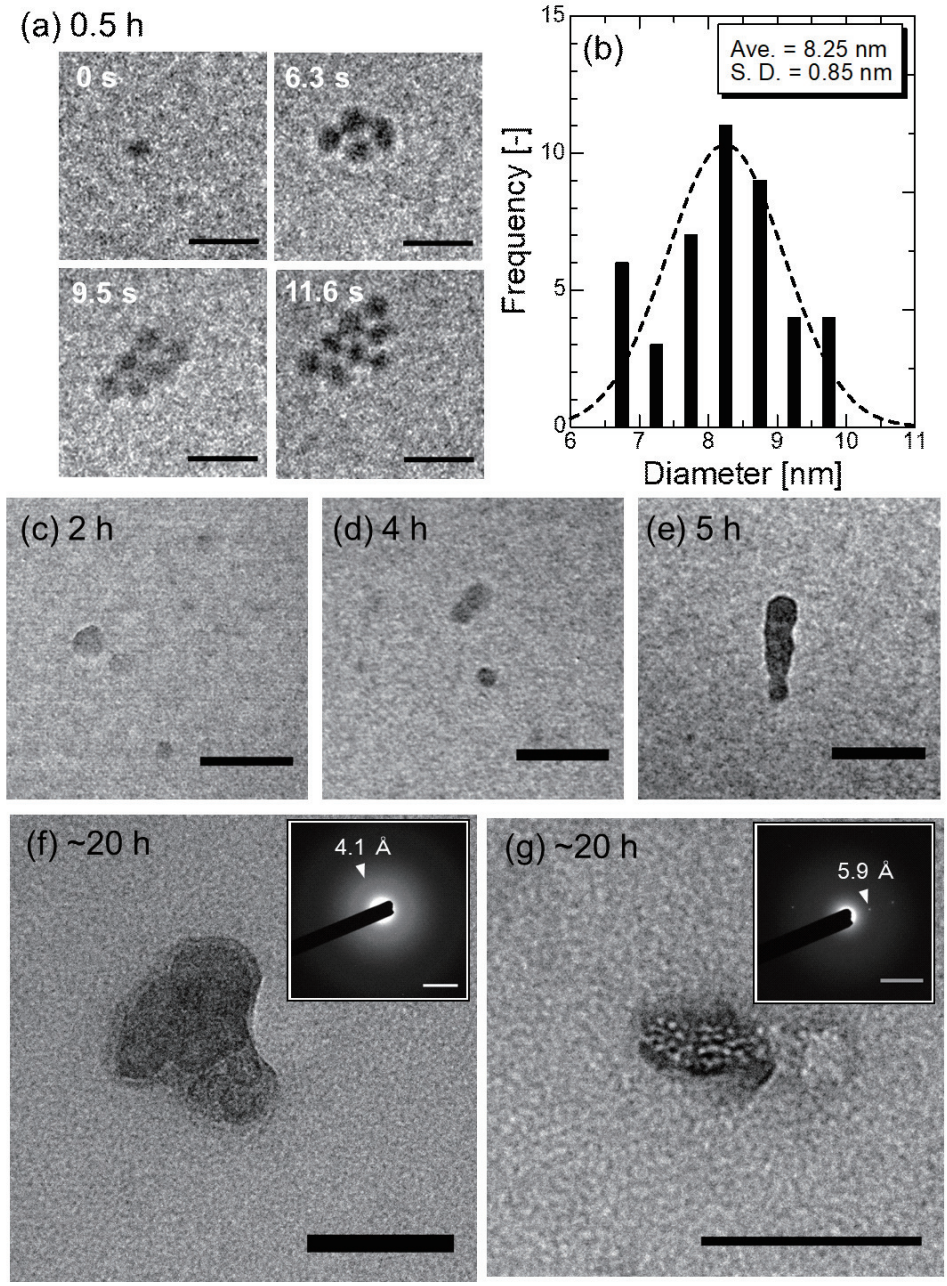

Figure 2: Evolution of aggregation of Aβ_{1-42} peptides. (a) Sequential snapshots of growth of the cluster consisting of dodecamers observed at ∼0.5 h. Scale bars denote 25 nm. Corresponding movie is Movie S3. (b) Distribution of the particle diameter. (The particle diameter was calculated from Movie S3.) The dashed line denotes the fitting curve drawn by the Gaussian function. (c)-(e) Evolution of aggregates composed of dodecamers from 2 to 5 h. The scale bars denote 100 nm. (f) and (g) TEM images of aggregates with ordered structures and corresponding ED patterns (insets) observed at ∼20 h. Scale bars in (f) and (g) denote 100 and 200 nm, respectively. Scale bars in their ED patterns denote 3 nm^{-1}. Images from (a) and (g) were taken at different positions.

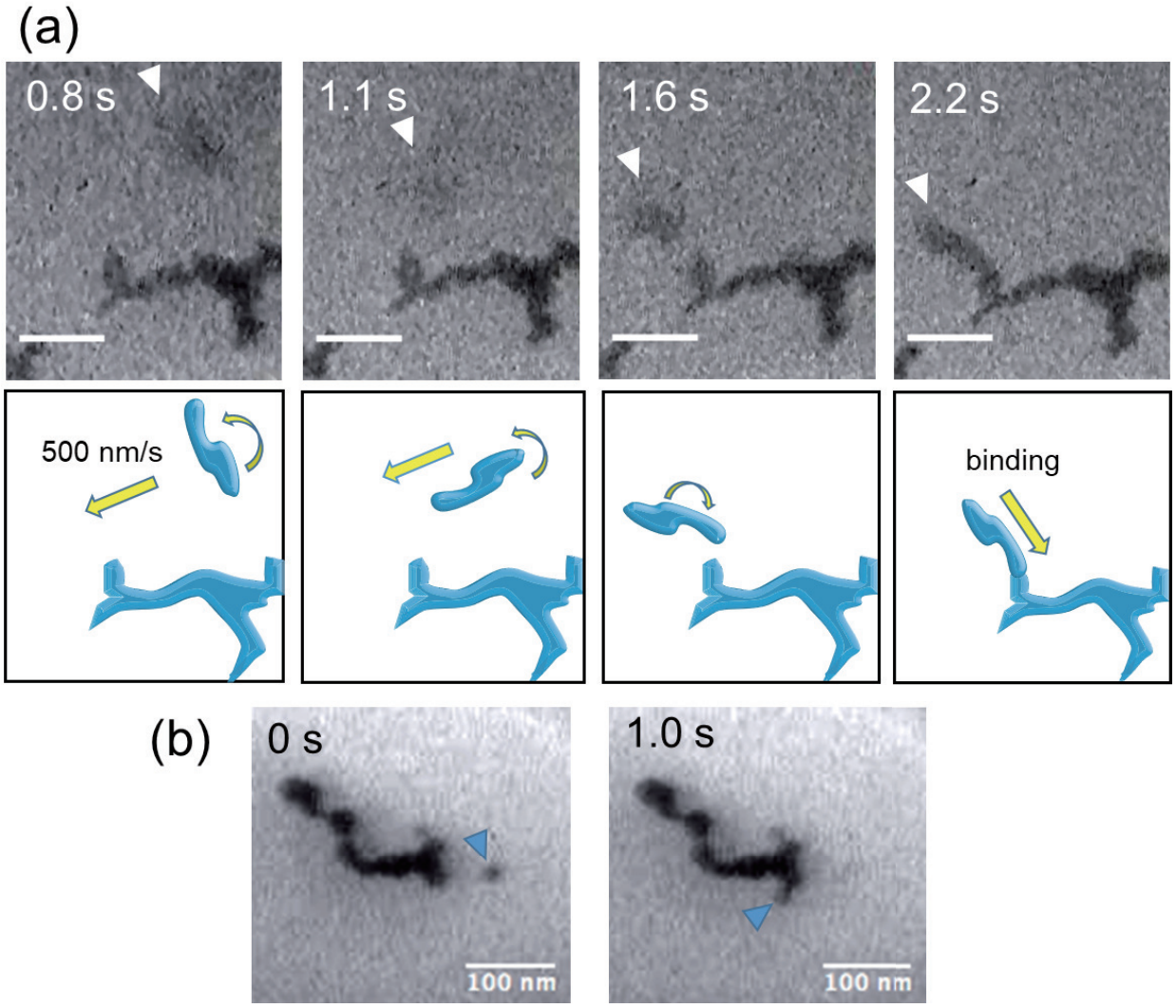

Figure 3: Highly specific long-distance interaction between Aβ_{1-40} oligomers. (a) Sequential snapshots of interaction between the moving stick-like aggregate and the branched aggregate, and corresponding schematics. The white arrow points the moving stick-like aggregate at each time. The corresponding movie is Movie S4. Scale bars denote 100 nm. (b) Snapshots showing the specific interaction of bead-like aggregates. The corresponding movie is Movie S5. The blue arrow denotes the small bead aggregate.

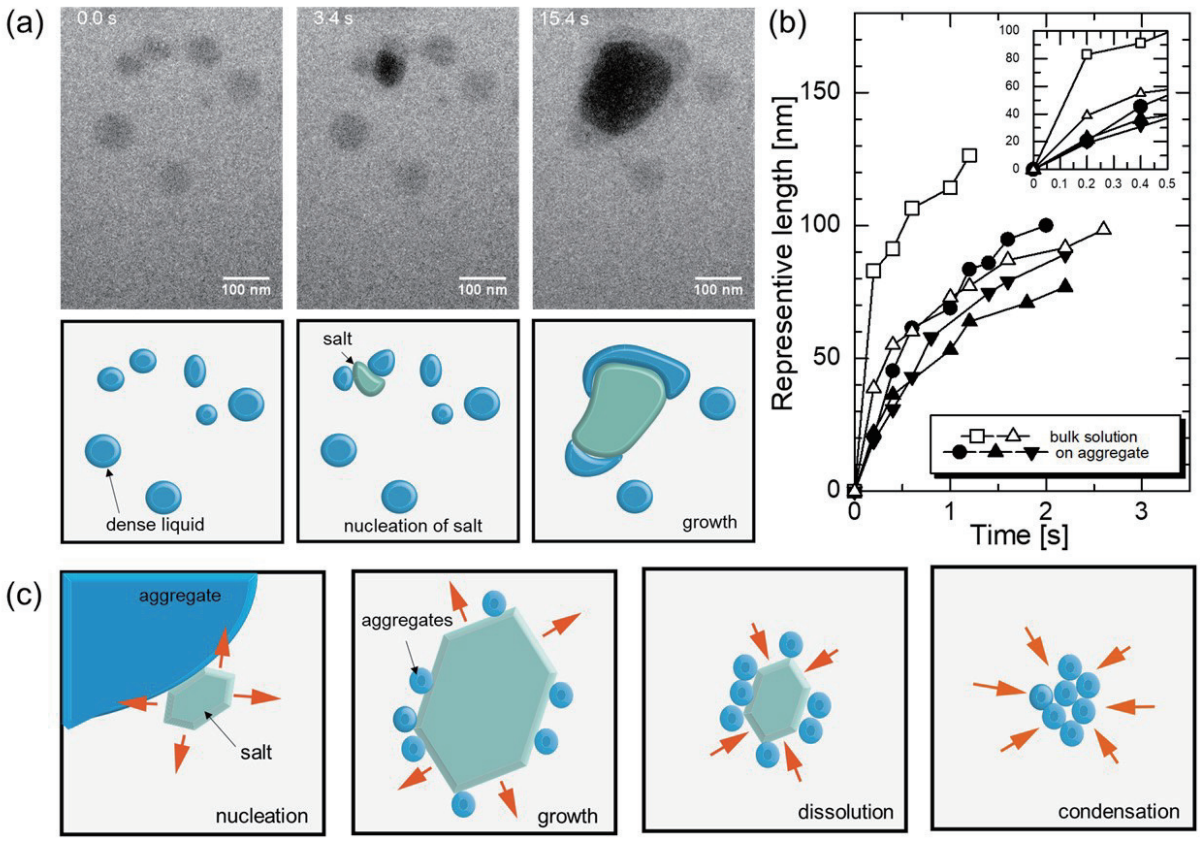

Figure 4: Cooperative Interaction between protein aggregation and salt crystal. (a) Sequential snapshots of TEM images during nucleation of a salt crystal by the surface of the dense-liquid droplet. The schematic illustration complementary explains this behavior. Corresponding movie is Movie S8. (b) Comparison of the growth behavior of NaCl crystal originated from bulk solution and from the surface of Aβ_{1-42} aggregate. (c) Schematic illustrations of the nanoscopic autocatalytic-like aggregation mechanism of Aβ peptides through the precipitation-dissolution event of a salt crystal.

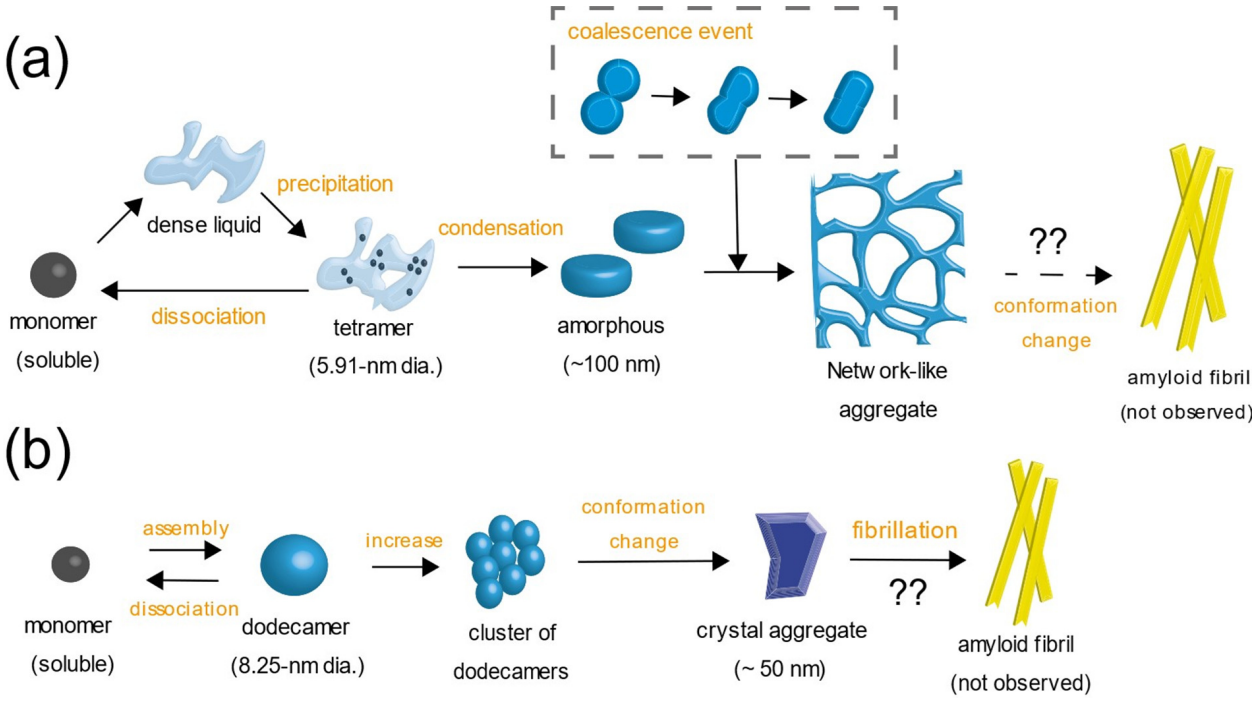

Figure 5: Schematic illustrations of early-stage evolutions of (a) Aβ_{1-40} and (b) Aβ_{1-42} oligomers.